Angewandte Chemie International Edition

Angewandte International Edition Chemie

GDCh German Chemical Society

How to cite: *Angew. Chem. Int. Ed.* **2026**, e23588
doi.org/10.1002/anie.202523588

RESEARCH ARTICLE

Nanocatalysts Built on Polypeptide Hybrid Materials: Towards Catalytic Versatility and Material Integration

Yuan Yao[1] | Xinyun Zeng[1] | Qi Mei[2] | Hang Xing[1] | Hui Wei[2] | Yugang Bai[1]

[1]State Key Laboratory of Chemo- and Bio-Sensing, School of Chemistry and Chemical Engineering, Hunan University, Changsha, Hunan, China | [2]College of Engineering and Applied Sciences, Nanjing National Laboratory of Microstructures, Jiangsu Key Laboratory of Artificial Functional Materials, Nanjing University, Nanjing, Jiangsu, China

Correspondence: Hui Wei (weihui@nju.edu.cn) | Yugang Bai (baiyugang@hnu.edu.cn)

Received: 27 October 2025 | **Revised:** 3 March 2026 | **Accepted:** 4 March 2026

Keywords: hybrid material | mixed matrix membrane | nanocatalyst | nanozyme | polypeptide

ABSTRACT

Nanozymes and many other types of nanocatalysts are emerging nanomaterials exhibiting high catalytic activity and robustness. Compared to natural enzymes, nanocatalysts have demonstrated advantages including cost-effectiveness, remarkable stability, and excellent durability. Yet, despite the substantial progress, nanocatalysts, especially nanozymes, are still facing critical limitations in catalytic diversity and material processability. In this article, we report a polypeptide-fused silica nanoparticle platform through an autocatalytic preparation strategy to simultaneously address both challenges. This nanocatalyst development system not only achieves the first example of nanocatalyst-mediated polypeptide synthesis, but also extends nanozymes' application scenarios to intracellular catalysis and membrane catalysis systems, expanding catalytic functionality while enabling convenient integration into other functional materials by improving nanozymes' processibility, as evidenced in the preparation and proof-of-concept application of nanozyme-bearing mix-matrix membranes (MMMs).

1 | Introduction

Nanozymes, as a representative type of nanocatalysts, have attracted increasing attention in multiple fields over the past two decades [1–6]. Their low preparation cost, robustness, and high catalytic activity have made them useful alternatives to enzymes in applications [7] where robustness and affordability are critical, for example, in rapid test kits [8], point-of-care platforms (POCTs) [9], in vivo disease monitoring [10], and the regulation of redox balance [11, 12]. However, behind the apparent prosperity of researches in nanozyme development and application, there is a widely acknowledged, core issue that deters the further progressing of this field: diversity in catalytic capability. Until now, a dominating majority [13] (>96%) of nanozymes reported are acting as mimics of peroxidase (POD) [14], superoxide dismutase (SOD) [15], catalase (CAT) [16], oxidase (OXD) [17], and glucose oxidase (GOx) [18]—this is in sharp contrast to the abundance in functionality for natural enzymes. Apparently, an expansion of nanozyme's catalytic repertoire is necessary, as more available transformations will surely bring usefulness of such nanocatalysts to more application scenarios, providing that the nanozyme's intrinsic advantages in robustness, activity and cost can be maintained.

A less frequently discussed but equally important challenge is the integration of nanozymes and other inorganic nanocatalysts into natural or synthetic functional systems. Enzymes are folded macromolecules, and those with good stability can be integrated into various functional materials, including but not limited to hydrogels [19–21], membranes [22, 23], liposomes [24, 25], textiles [26, 27], electrodes [28], even whole-cell catalysts [29], through covalent functionalization, fusion, and supramolecular

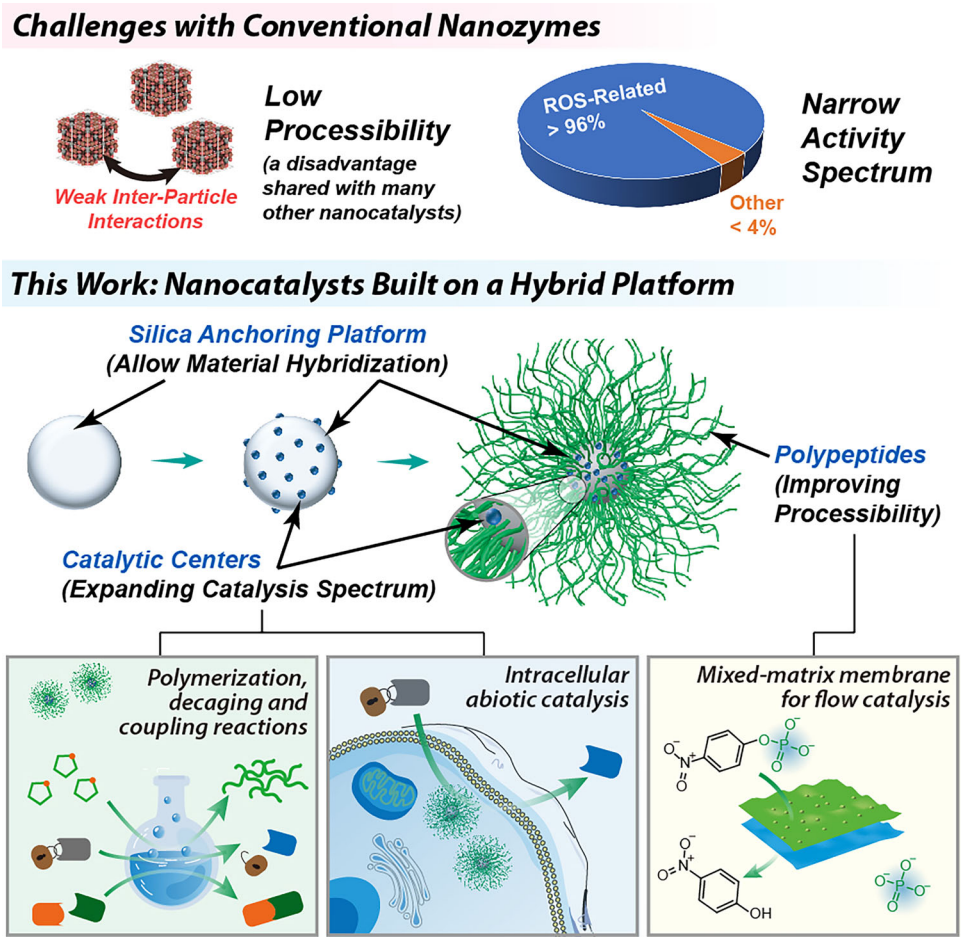

FIGURE 1 | A comparison of conventional nanozymes and the novel peptide-hybridized nanocatalyst platform reported in this work.

interactions. In contrast, nanozymes and many nanocatalysts are inorganic nanoparticles in nature and their colloidal stability and processibility can be extra issues, despite that their inorganic nature brings them higher robustness than those natural enzymes. Although their surfaces can be modified through ligand exchange [30] but the options are limited and the ligand-nanocatalyst association may not be durable. Unlike enzymes that are usually limited by their stability in material-oriented applications, nanozymes and most other types of nanocatalysts are not questioned on stability but troubled by their processibility and limited way of material integration. New strategies and development platforms are in absolute demand so that they can fully utilize their advantage in stability in diverse applications.

Here we present a strategy as a potential 2-in-1 solution for nanocatalysts, simultaneously enhancing their versatility in catalysis and granting them higher processibility for material integration (Figure 1). This strategy is built on the well-known silica nanoparticles (SiO_2NP) but furnished with polypeptide hybridization through autocatalysis-aided preparation protocols. This hybrid material platform not only brings easy incorporation of new catalytic functions, including the first case of nanocatalyst-mediated polypeptide preparation, but also viability in material integration, as illustrated in a nanozyme-bearing MMM for pollutant removal in water. This simple, easily prepared SiO_2NP@polypeptide hybrid scaffold is likely an attractive and useful platform for nanocatalyst development, enhancing their versatility and processibility to make them viable in diverse application scenarios not attempted before.

2 | Results and Discussion

2.1 | Autocatalysis-Aided Preparation of the Silica-Polypeptide Platform

To achieve the "2-in-1" solution for nanocatalyst versatility and processibility for system integration, we believe that a development platform is needed. This platform should be (1) nanosized for being called a nanocatalyst, (2) ready to accommodate various inorganic catalytic centers; and (3) bearing stable, functionalized shells for function integration and processibility. We consider SiO_2NP a suitable platform for this purpose. The well-known Stöber process has been a properly well-practiced way to prepare SiO_2NP with high size controllability at low cost, allowing the resulting SiO_2NP to be decorated with different functional groups available for post-modifications [31, 32]. In addition, the richness of Si—OH moieties on SiO_2NP makes them excellent anchors for a wide range of metals and metal oxides, through the formation of Si—O—M bonds. With these intrinsic features, one can confidently build catalytic systems on SiO_2NP using a broad spectrum of metal species of interest, and utilize the functional decorations on the SiO_2NP surfaces to integrate them into complex systems.

We thus performed the classical Stöber synthesis utilizing tetraethyl orthosilicate (TEOS), ethanol, and ammonium hydroxide. As anticipated, well-defined SiO_2NP of different sizes were obtained using this approach (100 nm to 800 nm) (Figure S1). We chose the SiO_2NP of median size (200–400 nm) as the model for the subsequent studies. Using 3-aminopropyl triethoxysilane (APTES), the prepared SiO_2NP could be further decorated with amino groups, and such modification was confirmed and quantified using ninhydrin (Figure S2). As a way of internal structure tuning, we also attempted to introduce porosity in the SiO_2NP, leading to the formation of mesoporous silica nanoparticle (MSN) core [33–35], by using cetyltrimethylammonium bromide (CTAB) as the structure-directing agent. Transmission electron microscopy (TEM) images (Figure 2c,d) revealed a uniform mesoporous architecture, and the observed pore diameter of 2.9 nm was consistent with the results from Barrett-Joyner-Halenda (BJH) pore size distribution analysis (2.3 to 2.7 nm, Figure 2e). X-ray diffraction (XRD) analysis revealed characteristic peaks for well-ordered mesoporous structure, including a prominent (100) diffraction peak at $2\theta \approx 2.05°$ and weaker (110) and (200) peaks (Figure 2f), collectively confirming long-range periodic ordering of the mesopores. Nitrogen adsorption–desorption measurements exhibited type IV isotherms, as shown in Figure 2g. The MSN could also be functionalized with amines using the aforementioned APTES method.

We then sought to construct a polymer-based shell for those SiO_2NP-NH_2, as polymer modification has been demonstrated as a viable way to improve the processibility of inorganic nanomaterials [36–41]. The strategy we used was to utilize the SiO_2NP-NH_2 as initiators for the ring-opening polymerization (ROP) of γ-benzyl-*L*-glutamate *N*-carboxyanhydride (BLG-NCA), yielding SiO_2NP@PBLG as the desired hybrid material scaffold. Unlike the traditional preparation methods for polypeptide-based materials, the synthesis of SiO_2NP@PBLG was facile, as it leveraged an autocatalytic mechanism reported by Cheng et al. [42–45]. The high density of amino groups on the SiO_2NP-NH_2, after ROP initiation, led to the formation of a dense array of polypeptide helices, which was reported to significantly promote the propagation of polypeptide chains within. Benefitting from such autocatalysis, this NCA-ROP-based shell construction process exhibited rapid polymerization kinetics (< 2 h, Figure 2h). Importantly, unlike the infamously difficult NCA-ROP, this autocatalytic, accelerated ROP allowed the use of crude NCA monomer under open-air conditions, making the system much more accessible for non-experts. Fourier-transform infrared spectroscopy (FT-IR) confirmed the presence of polypeptides on the SiO_2NP-NH_2 (Figure 2i), and we were also able to place the SiO_2NP@PBLG complex in HF acid to degrade the silica core for the characterization of the isolated polypeptides. Through gel permeation chromatography (GPC) characterization, we observed the narrow molecular weight distribution of the surface polypeptides which confirmed the uniformity of the polymer modification on the particle surface (BLG-NCA/SiO_2NP-NH_2 = 1:1 m/m, Figure 2j). Circular dichroism characterization revealed that these polypeptides were indeed adopting a helical structure in DCM (Figure S3). These data together suggested that the surface PBLG should be identical to those prepared using other polymerization methods. Scanning electron microscopy (SEM) and TEM revealed intact, aggregation-free spherical morphology of the NP@PBLG after NCA-ROP (Figure 2k). Based on CHON elemental analysis of SiO_2NP@PBLG and GPC characterization data of the cleaved PBLG, the average PBLG density on SiO_2NP was calculated to be 1 chain per ~400 nm^2. The system worked similarly when the core was changed to amine-modified MSN, giving MSN@PBLG. These results marked the success in building the nanocatalyst development platform based on a polypeptide-silica hybrid material.

2.2 | A Nanocatalyst Promoting Facile Polypeptide Preparation

The plain SiO_2NP@PBLG, without the introduction of any metal species into the core, was found to be a novel nanocatalyst that mediates NCA polymerization. Such catalytic activity is not surprising, considering the known NCA-ROP acceleration mechanism: the polypeptide chain propagation can be significantly promoted by the cooperative macrodipole created by the neighboring polypeptide α-helices in solvents with low dielectric constants, as we had just utilized in the preparation of the very SiO_2NP@PBLG material. We proceeded to study this nanocatalyst's activity in detail, using the d = 400 nm SiO_2NP@PBLG as the model (Figure S4). All the excess amino groups on SiO_2NP@PBLG, either on the silica core or on the PBLG's chain-end, were capped by acetic anhydride so that they would not interfere with the NCA-ROP. This nanocatalyst was mixed with BLG-NCA in dichloromethane (DCM) at a 1:1 mass ratio, followed by the addition of benzylamine as the initiator (M/I = 200). FT-IR monitoring revealed a fast decrease in anhydride peaks (1860 and 1790 cm^{-1}) from BLG-NCA (Figure 3b), reaching 80% conversion within 80 min (Figure 3c). At the same time, increased intensity in amide peaks at 1652 and 1550 cm^{-1} was observed, suggesting the formation of PBLG (Figure S5). The formed polypeptide could be easily separated from the SiO_2NP@PBLG catalyst by centrifugation and characterized by GPC (Table 1, **Entry 1–2**), and GPC analysis showed the dispersity remained low during the whole polymerization process (Figure 3d). Meanwhile, the PBLG chains on SiO_2NP@PBLG catalyst maintained their helical structure during the polymerization process, according to circular dichroism (CD) measurements (Figure S6). Importantly, mass spectrometry confirmed the ROP was initiated by benzylamine, not water or the nanocatalyst, as seen in Figure 3e. Interestingly, the ROP of BDG-NCA was also catalyzed by SiO_2NP@PBLG (Table 1, **Entry 4**), indicating that the key of catalysis was the macrodipole created by the helix array, but the absolute chirality of the helix should not matter much — the macrodipole is a simple vector without chirality. The ROP of racemic BDLG-NCA, however, was not helped by SiO_2NP@PBLG (Figure 3f), because the corresponding polymer product could not form a helix to "enjoy" the macrodipole. In a more detailed study (Figure S7), the data suggested that both the helical polypeptides on the NP surface and the polypeptides from NCA-ROP might contribute macrodipole needed for the catalytic effect, which is, in the very nature, analogous to that observed in cooperative covalent polymerizations (CCPs) [46].

The highly active nature of this nanocatalyst was indicated in its efficient removal of the stringent conditions required by traditional NCA-ROP. With this nanocatalyst, the ROP became highly tolerate to moisture and other impurities. The traditional amine-initiated NCA-ROP typically requires repeated

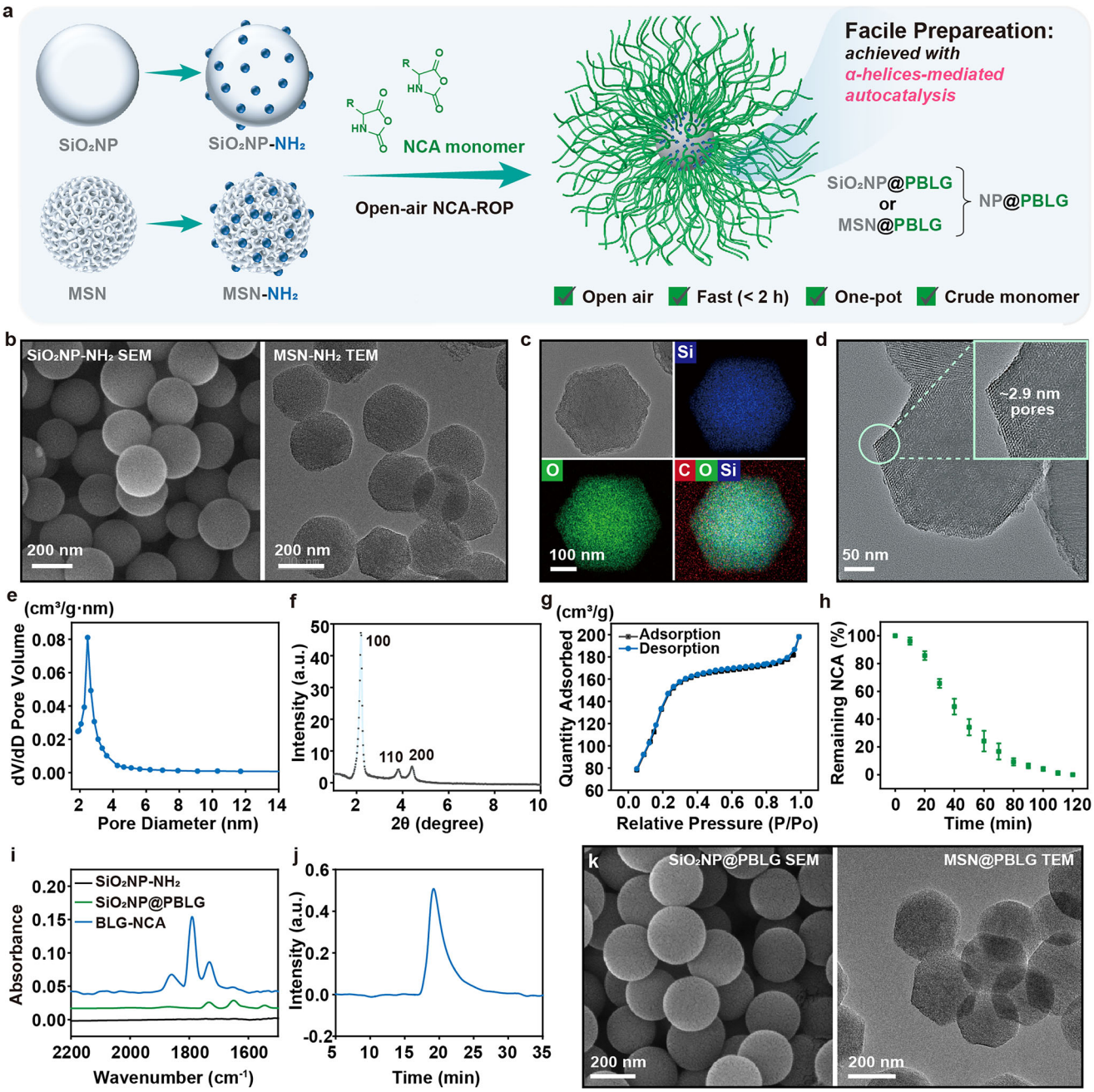

FIGURE 2 | (a) Schematic illustration of the autocatalysis-aided preparation of the NP@PBLG nanocatalyst development platform. (b) Images of SiO_2NP-NH_2 (left) and MSN-NH_2 (right). (c) Elemental mapping of C, O and Si of MSN@PBLG obtained using scanning transmission electron microscopy coupled with energy dispersive x-ray spectroscopy (STEM-EDX). (d) TEM visualization of the pores on MSN-NH_2. (e) BJH pore size distribution analysis of MSN-NH_2. (f) XRD characterization result of MSN-NH_2. (g) N_2 adsoprtion–desoprtion isotherms measured at 77 K on calcined MSN-NH_2. (h) Kinetic study of BLG-NCA's polymerization on SiO_2NP-NH_2 using IR spectroscopy. (i) FT-IR analysis showing the PBLG was successfully grafted onto SiO_2NP by NCA-ROP. (j) GPC characterization of the surface polypeptides after they were detached from the silica cores using HF/DCM (1:3 v/v). $M_n = 3.5\times10^6$ Da, $Đ = 1.26$. (k) SEM visualization of SiO_2NP@PBLG (left) and TEM visualization of MSN@PBLG (right).

NCA recrystallization before monomer usage, but with this SiO_2NP@PBLG nanocatalyst, the ROP could be done in open-air using monomers obtained directly from a simple precipitation work-up and benchtop solvent (Figure 3g,h, Table 1, **Entry 5–10**). Apparently, this significantly reduced the difficulty and time needed for polypeptide preparation. Another monomer, ZLL-NCA, was seen compatible with this catalyst as well (Table 1, Entry 3 and 6, Figure S8), and copolymerizations could be performed, too, through sequential monomer addition (Table 1, **Entry 11–12,** Figure S9, S10). Other initiators including small molecules and polymers also worked (Figure S11). For example, a poly(ε-caprolactone) (PCL) macroinitiator, PCL-S-S-NH_2, could lead to the formation of a hybrid copolymer with BLG-NCA and the nanocatalyst, and the copolymer could form micelles after the PBLG segments' side-chains were deprotected (Figure S12). Importantly, being a heterogeneous catalyst in nature, the SiO_2NP@PBLG nanocatalyst exhibited excellent recyclability (Figure 3i). After being isolated by centrifugation, it could be

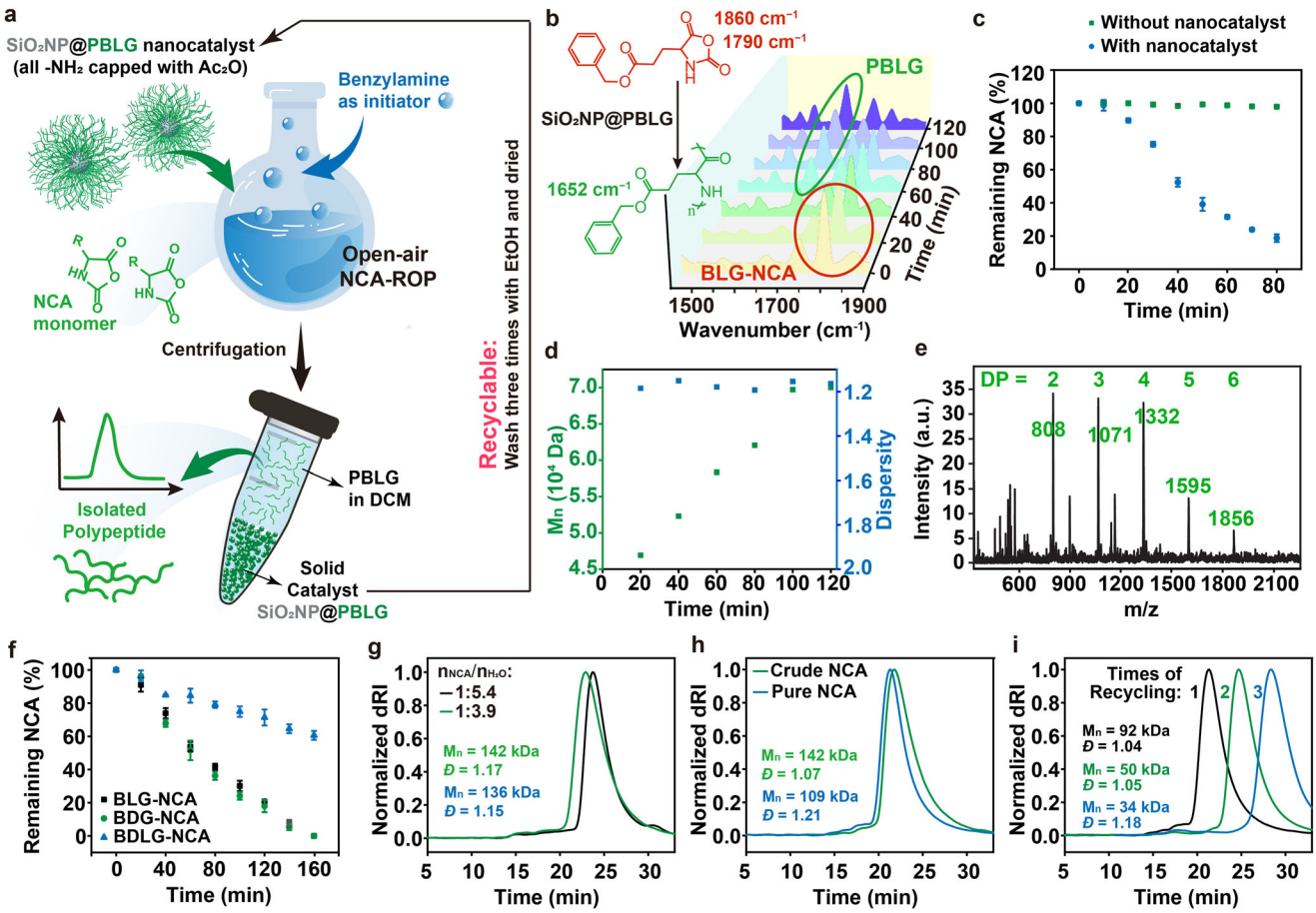

FIGURE 3 | (a) A schematic illustration of the open-air polymerization of NCA monomers, mediated by the recyclable SiO_2NP@PBLG nanocatalyst. (b) IR spectra overlay of the reaction mixture during the ROP of BLG-NCA mediated by SiO_2NP@PBLG. SiO_2NP@PBLG was removed before taking each IR spectrum. (c) Comparison of the kinetics of BLG-NCA's polymerization in the presence or absence of the SiO_2NP@PBLG nanocatalyst. (d) Number-average molecular weight (M_n) and dispersity of PBLG obtained at 20–120 mins after initiation, catalyzed by SiO_2NP@PBLG. (e) MALDI-TOF MS spectrum of low molecular weight PZLL obtained from benzylamine-initiated NCA-ROP catalyzed by SiO_2@PBLG. The observed m/z values matched the theoretical values: $m/z = 262.13 \times DP + 154.03$ (DHB) + 107.07 (Benzylamine) + 22.99 (Na). The polymerization was quenched shortly after initiation. (f) Comparison of BDG-, BLG-, and BDLG-NCA's polymerization kinetics when SiO_2NP@PBLG was utilized as the catalyst, revealed by IR spectroscopy. (g) GPC characterization of PBLG obtained from SiO_2NP@PBLG-catalyzed ROP with the presence of added water, which showed the robustness of the catalysis. (h) GPC characterization of PBLG obtained from SiO_2NP@PBLG-catalyzed ROP of crude BLG-NCA monomer. The crude NCA was obtained directly from petroleum ether precipitation after phosgenation, while the pure NCA was obtained by repeated recrystallization. (i) GPC characterization of PBLG obtained using SiO_2NP@PBLG that was recycled once, twice and thrice. For all the polymerizations above, benzylamine was used as the initiator ($M/I = 200{:}1$), and m(NCA)/m(SiO_2NP@PBLG) was kept at 1:1.

washed and dried for reuse for multiple times. Collectively, these results demonstrated the excellent activity and robustness of SiO_2NP@PBLG as a novel NCA-ROP nanocatalyst.

2.3 | Immobilization of Metal Catalytic Centers in the MSN@PBLG Platform

The above NP@PBLG platform, in addition to its capability of serving as a polymerization nanocatalyst itself, can be conveniently endowed with other catalytic abilities by depositing different metal species onto the silica core [47]. To facilitate the metal deposition process, we used MSN as the core, for it has a higher surface area and porosity. A model system was established through the reduction-deposition of sodium chloropalladate to metallic palladium on MSN-NH_2 using sodium borohydride. With a Na_2PdCl_4/$NaBH_4$/MSN-NH_2 mass ratio of 80:21:50, a palladium-loaded NP, MSN(Pd)-NH_2, was obtained. NCA-ROP was then performed on the surface of MSN(Pd)-NH_2, and the resulting nanocatalyst, MSN(Pd)@PBLG (Figures S13, S14), showed good dispersibility in aqueous environment, while the common Pd/C catalyst only formed precipitates (Figure 4b). The Pd loading rate of MSN(Pd)@PBLG was determined to be adjustable (~5% to 13%) by ICP-MS. The nanocatalyst was then evaluated for its catalytic performance in the Suzuki coupling reaction, using 1-iodo-4-methoxybenzene (**S1**) and 2-phenylthiazole (**S2**) as the fluorogenic substrates for convenience. Fluorescence (Figure S15) and HPLC peak of the product was clearly observed in 20 h (yield 73%, Figures 4c and S15, S16), confirming the catalytic ability of the MSN(Pd)@PBLG nanozyme. The reaction also featured Michaelis-Menten-type kinetics (Figure S17), identifying the MSN(Pd)@PBLG nanocatalyst a nanozyme. Encouraged by these results, we went on to evaluate if such nanozyme with modularly added catalytic

TABLE 1 | NCA polymerizations initiated by benzylamine with SiO_2NP@PBLG nanocatalyst.

Entry[a]	NCA	*M*/*I* ratio[b]	Solvent	M_n (kDa)/DP	Dispersity
1	BLG	200:1	DCM	142.3 (650)	1.07
2	BLG	50:1	DCM	84.15 (384)	1.05
3	ZLL	200:1	DCM	71.63 (272)	1.15
4	BDG	200:1	DCM	132.4 (605)	1.13
5	BLG	200:1	DCM (ND)[c]	141.6 (646)	1.17
6	ZLL	200:1	DCM (ND)[c]	49.90 (190)	1.11
7	BDG	200:1	DCM (ND)[c]	126.10 (576)	1.16
8	Crude BLG[d]	200:1	DCM	109.5 (500)	1.21
9	Crude BDG[d]	200:1	DCM	100.5 (459)	1.22
10	Crude ZLL[d]	200:1	DCM	57.80 (220)	1.09
11	BLG-*co*-ZLL[e]	200:86:1	DCM	607.9 (1849:774)[g]	1.05
12	BLG-*b*-ZLL[f]	200:34:1	DCM	263.6 (1003:167)[g]	1.11

[a]For the entries not noted otherwise, DCM was dried using molecular sieves and monomers were purified through repeated recrystallization.
[b]For all polymerizations, benzylamine was used as the initiator, and a 1:1 (w/w) ratio of NCA/nanocatalyst was used.
[c]DCM was taken directly from commercial containers and was not dried before use.
[d]The crude monomers were obtained by directly pouring the reaction solution into the petroleum ether, collected by filtration and vacuum-dried.
[e]Random copolymerization using BLG-NCA (20 mg) and ZLL-NCA monomer (10 mg), 2 h reaction time.
[f]Block copolymerization by sequential addition of BLG-NCA monomer (25 mg) and ZLL-NCA monomer (5 mg), 1 h reaction time for each block.
[g]The ratio of BLG and ZLL residues on the copolymers, determined by ^{1}H NMR. The peaks for the methylenes on the benzyl groups were used for integration and quantification (peak deconvolution was required).

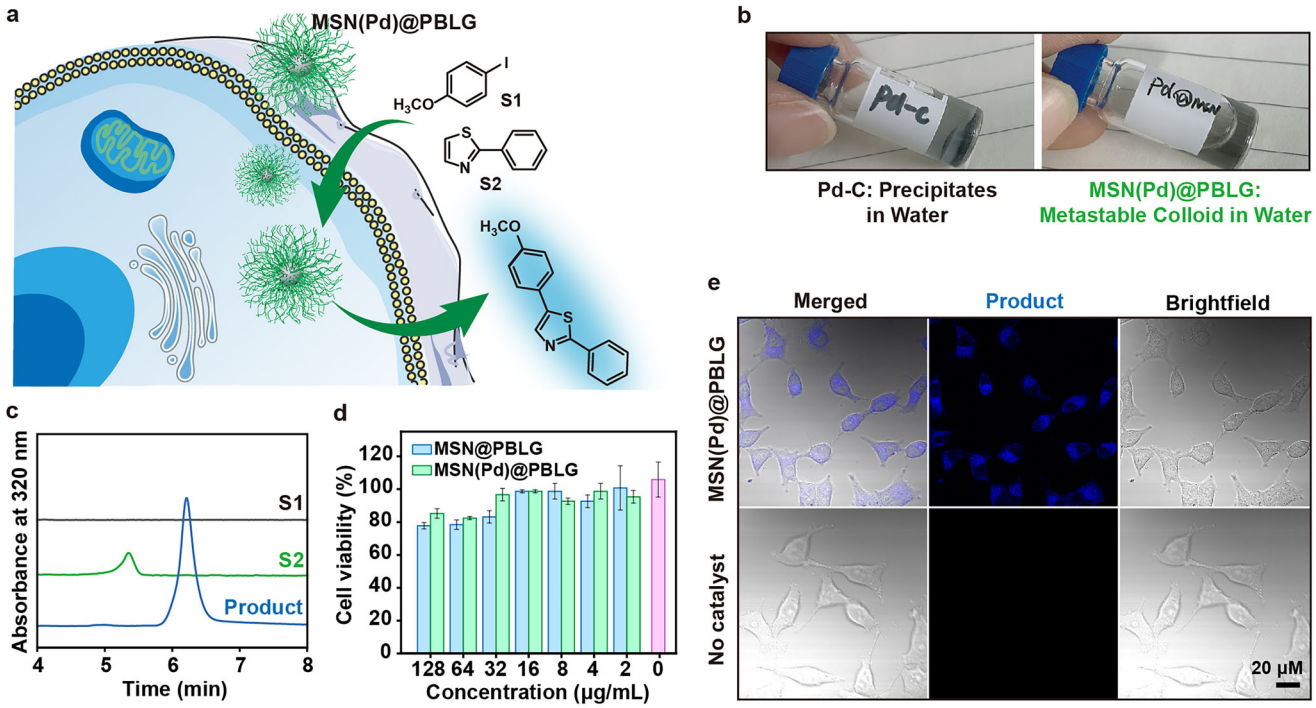

FIGURE 4 | (a) A cartoon illustration of intracellular Suzuki coupling reaction mediated by MSN(Pd)@PBLG nanozyme. (b) Photos showing the difference in colloidal stability of commercial Pd-C catalyst and MSN(Pd)@PBLG in PBS. (c) HPLC chromatogram overlay showing the formation of the product, from the MSN(Pd)@PBLG-mediated Suzuki coupling of **S1** and **S2** in PBS. Mobile phase: CH_3OH (0.1%TFA) and H_2O (0.1%TFA) gradient, 1.0 mL/min. (d) MTT assay result showing the cell viability using MCF-7 cells treated with MSN@PBLG or MSN(Pd)@PBLG at different concentrations. (e) Confocal microscope visualization of the fluorescent product formed inside MCF-7 cells. The intracellular Suzuki coupling was mediated by MSN(Pd)@PBLG (5 μg/mL) with [**S1**] = 100 μM and [**S2**] = 110 μM.

capability could potentially be used in a biological environment like many other ROS-related nanozymes reported before. After having validated the successful cell uptake of these polymer-coated, slightly negatively charged NPs (Figure S18), we incubated MCF-7 cells with MSN(Pd)@PBLG; and after the cell uptake of the nanozymes, the cells were then incubated with the same fluorogenic reactants, 1-iodo-4-methoxybenzene and 2-phenylthiazole. After 6 h, confocal microscopy clearly revealed the cyan fluorescence from the product in the treated cells, indicating excellent intracellular catalytic activity of the nanozyme (Figure 4e). Importantly, we also assessed the cytotoxicity of MSN(Pd)@PBLG using MTT assay, which revealed that this material had an excellent biocompatibility profile, showing >80% viability of the cells at a concentration of ≤ 128 μg/mL (Figure 4d).

Alternatively, the introduction of catalytic centers could be done by simple cofactor trapping instead of a redox-deposition process. This was exemplified by changing the Pd to Cu for the catalysis of Cu(I)-catalyzed azide-alkyne 1,3-cycloaddition (CuAAC). By simply incubating Cu-BTTAA complex with MSN-NH_2, the complex could be trapped in the pores of the nanoparticles (>10% wt loading), and then the NP was transformed into MSN(Cu)@PBLG by surface-initiated NCA-ROP (Figure S19). This nanocatalyst was also able to mediate abiotic reaction in live MCF-7 cells, turning 3-azido-7-hydroxycoumarin and *p*-ethynylanisole into a fluorescent coumarin derivative (Figures S20, S21). Regardless of the way used to introduce metal centers, we believed that the PBLG shell had helped in increasing the local concentration of the substrates, therefore increasing the overall reaction rate. This was demonstrated by a simple experiment in which organic dyes were incubated with MSN@PBLG in water, and UV–vis spectroscopy revealed that a significant amount of dyes were captured by the nanocatalyst (Figure S22). From these results, one can see the potential of this modular nanocatalyst platform in diverse biomedical and chemical biology applications by creating new bioorthogonal pathways in live cells, which may make this NP@PBLG platform intrigue researchers of many different fields.

2.4 | Improved Processibility of the MSN@PBLG Scaffold Enables Functional MMM Preparation

As inorganic material, many nanocatalysts have intrinsically low processibility, which makes it difficult to integrate them into other functional matrices. While surface coating is a common way to improve the processibility of inorganic nanoparticles, such coating can potentially devastate the catalytic performance of nanocatalysts as the coating can disrupt the key structures of the nanocatalyst surfaces. Our NP@PBLG scaffold, however, provides a unique opportunity for processibility enhancement of nanocatalysts, as the PBLG chains rooted on the silica can themselves serve as coatings without disrupting the nanocatalyst's activity. To demonstrate this feasibility, we started a MMM preparation attempt using MSN@PBLG (Figure 5a). The MSN@PBLG scaffold (M_n = 2.0×10^5 Da, $Đ$ = 1.18 for BLG-NCA/MSN-NH_2 = 1:1 m/m, d_{MSN} = 400 nm, Figures S23, S24) was synthesized through in situ NCA-ROP initiated by MSN-NH_2 of the corresponding size, as previously demonstrated. The freshly synthesized MSN@PBLG in chloroform solution was directly cast onto a Nylon membrane. Subsequent solvent evaporation facilitated robust interfacial adhesion between MSN@PBLG and Nylon, presumably mediated by the polar interactions and hydrogen bonding between Nylon and PBLG, both of which are polyamides. Notably, the PBLG modification ensured homogeneous dispersion of MSN in the polymer matrix of the resulting Nylon-MSN@PBLG MMM (Figure 5b), and the membrane was stable toward folding, even after 30 h of continuous water flow (Figure S25). In contrast, MSN itself could not form a stable MMM on Nylon, but behaving more like loosely packed powders that broke upon folding (Figure 5b). When simple PBLG/MSN mixture (instead of the covalently linked composite MSN@PBLG) was used for MMM preparation, it also gave better membrane than using MSN only, but the roughness of the formed MMM in this way clearly indicated lower structure uniformity compared to the MMM prepared with MSN@PBLG. Morphological characterization of the membranes via scanning electron microscopy (SEM) revealed substantial structural differences. Nylon-MSN "membrane" was actually loosely packed nanoparticles under SEM, and its fragility was already indicated in the folding test. Meanwhile, although the Nylon-(MSN+PBLG) MMM demonstrated improved stability compared to Nylon-MSN, it clearly showed fractures in the cross-section, but the Nylon-MSN@PBLG featured uniform cross-sectional morphology. This observation was consistent with the apparently rougher surface of Nylon-(MSN+PBLG) MMM (Figure 5b). We also checked how the BLG-NCA/MSN-NH_2 ratio would affect the MMM preparation, and it was seen that ratios between 5:1 to 1:1 were giving satisfactory results (Figure S26).

We then went on to evaluate if such integration of the nanocatalyst scaffold could possibly affect the intrinsic functionality of the core. This was done by assessing the MMM's molecule absorption performance, which is the inherent function of the porous MSN core. For this purpose, hydrophobic, and hydrophilic organic dyes, namely methylene blue (MB), BODIPY and Thioflavin T (THT), as well as a common metal salt contaminant, $K_2Cr_2O_7$ (Figure 5c), was dissolved in water and made passing through the MMMs prepared above. The Nylon-MSN "membrane" was not included because of its low viability due to extremely high fragility. It was observed clearly that the Nylon-MSN@PBLG could successfully leverage the intrinsic porosity of MSN, enabling the efficient removal of small molecules and ions from the solutions (Figure 5d,e). In contrast, the Nylon-(MSN+PBLG) MMM and Nylon-PBLG MMM failed to do any filtration as it proved to be completely water-impermeable, likely due to the high hydrophobic nature brought in by PBLG. Collectively, these findings not only demonstrated the improved processibility enabled by the NP@PBLG scaffold that can potentially enhance nanocatalyst integration into other functional materials, but also validated that the improved processibility was made possible not at the cost of functionality. The functionality at the nanocatalyst core could be well maintained, as revealed in the above MMM preparation.

2.5 | Nylon-MSN(CeO_2)@PBLG MMM as a Nanozyme-Empowered Pollutant Removal Tool

As we have shown that the MSN@PBLG scaffold could be easily integrated into functional materials, such as an MMM, we moved to establish a proof-of-concept demonstration, in which modularly introduced nanozymes could be processed along with

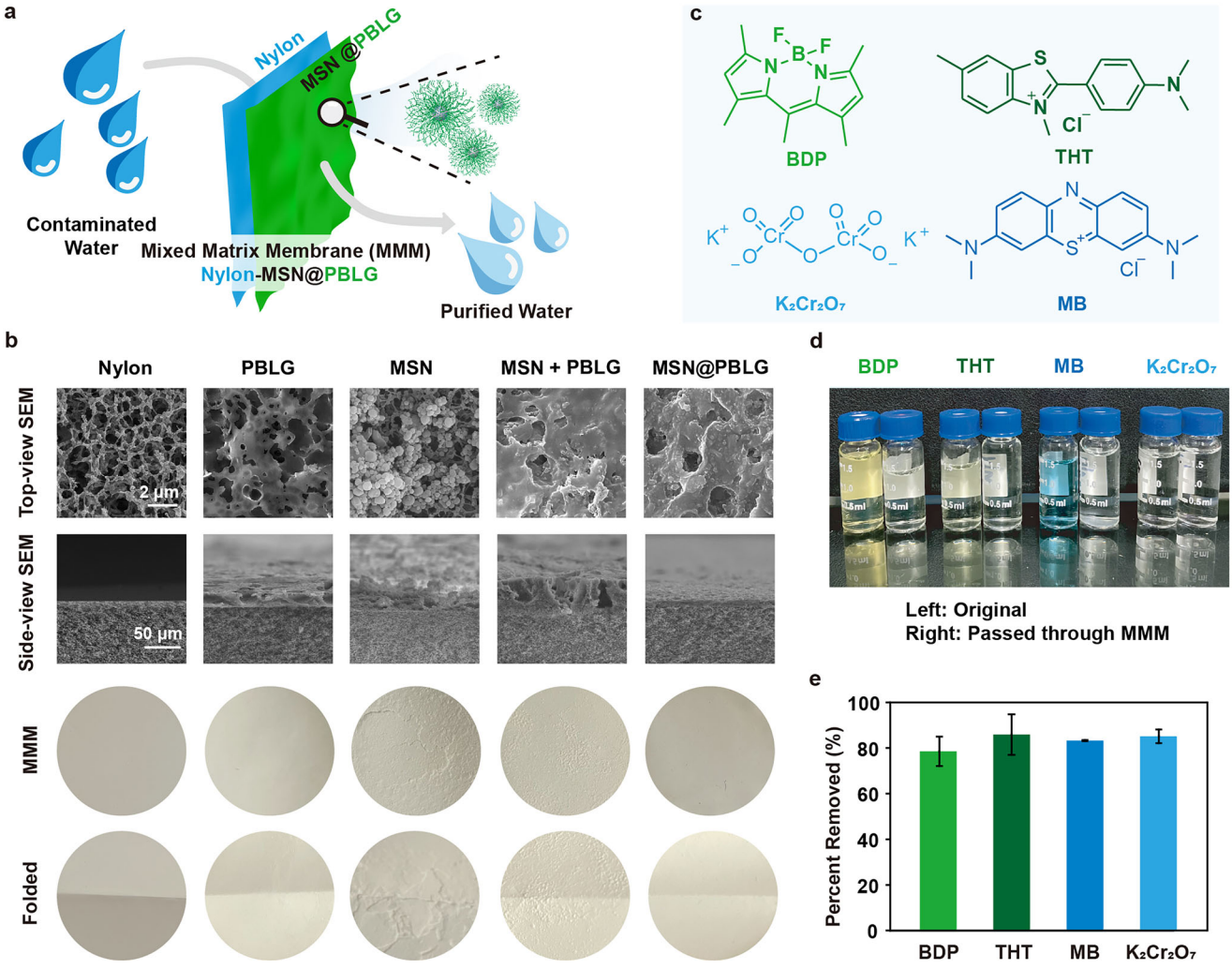

FIGURE 5 | (a) A cartoon illustration on the working mode of Nylon-MSN@PBLG MMM for pullutant removal in water. (b) The top- and side-view SEM images of the MMM, and photographs of the prepared MMM before and after folding test. (c) The chemical structures of BODIPY, THT, methylene blue, and $K_2Cr_2O_7$, used as model pollutants in water. (d) Photos showing the strong molecular absorption effect of the prepared Nylon-MSN@PBLG MMM. (e) Quantification of the dye/metallate removal efficiency by passing the aqueous solutions through the prepared Nylon-MSN@PBLG MMM. Nylon-(MSN+PBLG) and Nylon-PBLG MMM were tested together but the filtrate was unable to pass through, so no result was obtained. Nylon-MSN was not tested because it was too fragile for any model study. Error bars represent ± SD.

the MSN@PBLG scaffold and function properly in a hybrid material matrix as proposed. We chose CeO_2 as the model nanozyme to be incorporated into the MSN@PBLG scaffold, for it has demonstrated exceptional phosphatase-like activity in biomedical applications, mediating efficient dephosphorylation under mild conditions [48, 49], including the detoxification of organophosphates. Meanwhile, CeO_2 is a metal oxide, facilitating its seamless integration with the silica core through Si-O-M bonding. We were expecting that the successful integration of CeO_2 nanozyme [50–55] could bring us a highly versatile MMM that could remove pollutants in water through both catalytic and absorptive pathways (Figure 6a).

The incorporation of CeO_2 units into the MSN@PBLG scaffold was achieved using a protocol similar to the preparation of MSN(Pd)@PBLG. In short, MSN-NH_2 was mixed with $Ce(NO_3)_3{\cdot}6H_2O$ in a mixture of ethanol, ethylene glycol, and ammonium hydroxide, and was heated to 100°C for the desired metal oxide to form and deposit on silica. The resulting MSN(CeO_2)-NH_2 were then subjected to in-situ polymerization to form MSN(CeO_2)@PBLG nanozyme composite (Figure S27). TEM characterization clearly revealed CeO_2 nanostructure formation on the MSN surface, and elemental mapping confirmed the successful deposition of Ce. The anchoring of Ce (and other) species on the MSN core was proved stable, as negligible leaching was identified after being placed 24 and 48 h in water (Figure S28). After optimizing the synthetic parameters, we selected the most effective catalyst (Table S1 and S2) for kinetic studies. A remarkably high conversion rate of nearly 70% was achieved within just 1 min using merely 2.4 mg of such MSN(CeO_2)@PBLG nanozyme (Figure 6b), demonstrating superiority to those traditional "standalone" CeO_2 enzymes of various morphologies (Figures 6b, S29 and Table S3). Thus, we continued to utilize the membrane fabrication technique described earlier, so that MSN(CeO_2)@PBLG was processed into an "catalytic MMM". ICP-MS analysis indicated a high Ce content of 11.1% in the resulting MSN(CeO_2)@PBLG nanozyme core. Similar to the Nylon-MSN@PBLG MMM described above, TEM imaging of the

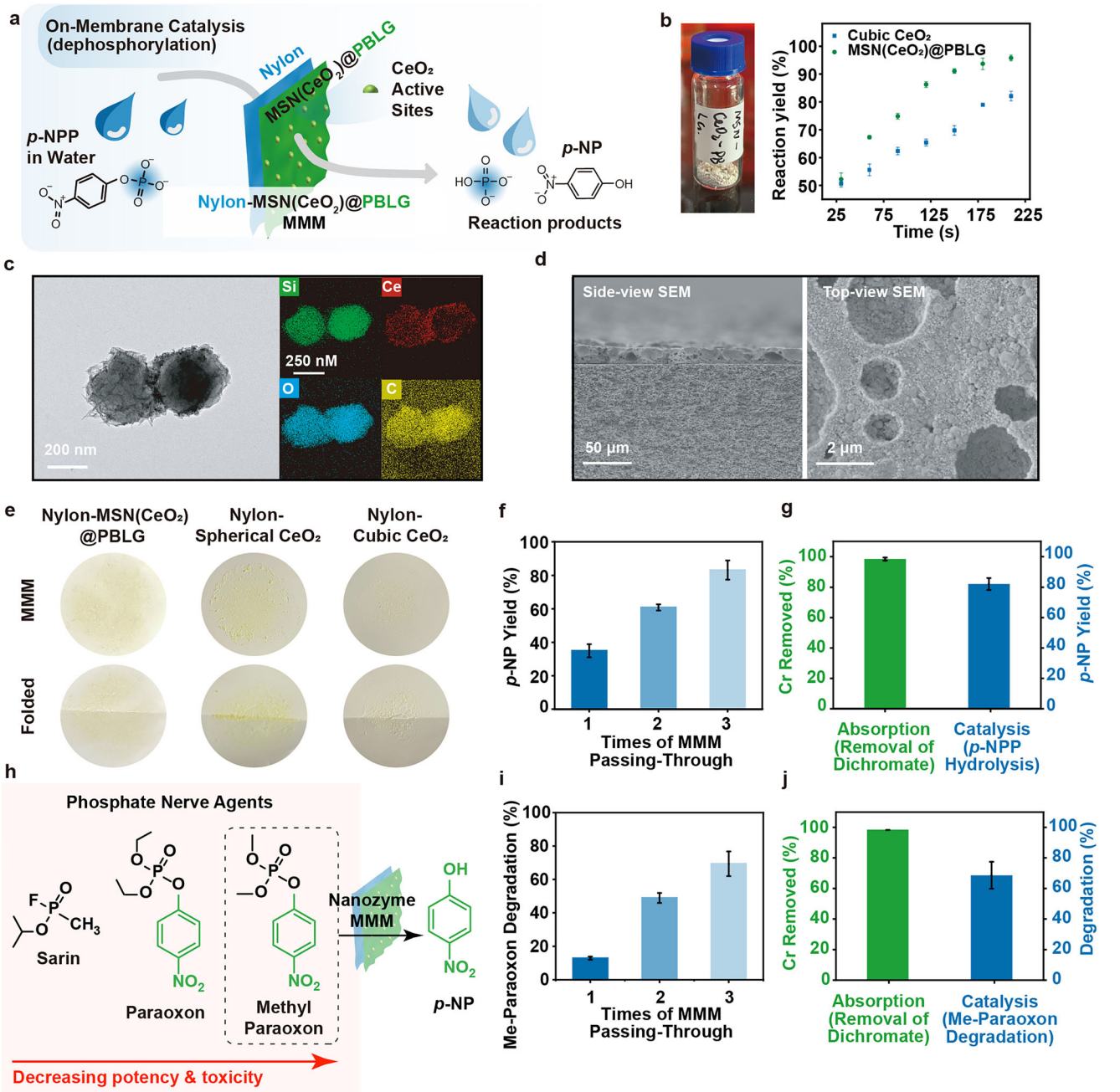

FIGURE 6 | (a) A cartoon illustration showing the on-membrane dephosphorylation catalysis mediated by the Nylon-MSN(CeO_2)@PBLG MMM, a nanozyme-integrated hybrid material. (b) Kinetic study of p-NPP hydrolysis catalyzed by Nylon-MSN(CeO_2)@PBLG powder through UV–vis spectroscopy. 65°C, $[p\text{-NPP}]_0$ = 30 μM. (c) TEM image and EDX elemental mapping of MSN(CeO_2)@PBLG nanostructures. (d) Top- and side-view SEM images of the Nylon-MSN(CeO_2)@PBLG MMM. (e) Photographs of the prepared Nylon-MSN(CeO_2)@PBLG MMM before and after the folding test. The fragile membranes prepared using CeO_2 nanozymes (of two different shapes) were shown as comparison. (f) UV–vis quantification of the on-membrane catalysis. Aqueous *p*-NPP solution (10 μM) was made flowing through MSN(CeO_2)@PBLG MMM at 65°C for 1–3 times. (g) ICP-MS/UV–vis quantification of Cr and *p*-NPP removal after a solution containing both $K_2Cr_2O_7$ (0.008 mg/mL) and *p*-NPP (10 μM) was made flowing through the MSN(CeO_2)@PBLG MMM three times. *p*-NPP conversion was determined by measuring the concentration of the hydrolyzed product, *p*-NP. (h) Structures of phosphate nerve agents, and a schematic diagram of methyl paraoxon degradation using Nylon-MSN(CeO_2)@PBLG MMM. (i) UV–vis quantification of the on-membrane catalysis for the degradation of methyl paraoxon (aq., 10 μM), which was passed through MSN(CeO_2)@PBLG MMM at 65°C, at pH = 10, for 1–3 times. (j) ICP-MS/UV–vis quantification of simultaneous $K_2Cr_2O_7$ (0.008 mg/mL) and methyl paraoxon (10 μM) removal by MSN(CeO_2)@PBLG MMM (3 passing-throughs). Percent of degradation was determined by measuring the concentration of the hydrolyzed product, *p*-NP.

fabricated CeO_2-containing MMM showed a nanocomposite layer stably adhered to the Nylon support (Figures 6d, S30). In contrast, the attempt to prepare MMM directly with CeO_2 NPs resulted in an unstable layer with rough surface morphology, and showing clear signs of detachment upon folding. Again, this phenomenon indicated that the MSN@PBLG scaffold was necessary to endow the nanozyme system with enough processibility for material integration, such as in the preparation of an MMM (Figure 6e).

Next, we employed *p*-nitrophenyl phosphate (*p*-NPP) as the model chromogenic substrate to evaluate the catalytic activity of the MMM in mediating dephosphorylation reaction when serving as a filtration device. Ideally, the high efficiency and turnover number of such nanozyme system can achieve a pass-to-degrade process, removing undesired phosphates in a very convenient way. Meanwhile, the MMM may also work as a pollutant absorbent, removing other unwanted molecules through trapping as we have indicated in the section above. Since both *p*-NPP and its hydrolysis product, *p*-NP (which converts to *p*-nitrophenolate at high pH) (Figure S31), exhibited distinctive UV–vis absorption spectra, real-time reaction monitoring could be performed conveniently. We observed that for a *p*-NPP solution of 10 μM, three consecutive MMM passing-throughs (flow rate ca. 5 mL/min) at 65°C would lead to >80% dephosphorylation (Figure 6f), demonstrating the robust catalytic efficiency of this nanozyme-integrated MMM under flow conditions. It should be noted that the incorporation of CeO_2 did not affect the intrinsic property of the MSN core. The MMM material demonstrated dual functionality, that is, molecular adsorption and catalysis. We challenged the system with a mixed solution containing both $K_2Cr_2O_7$ (0.008 mg/mL, as a model heavy metal pollutant) and 10 μM *p*-NPP. Remarkably, concurrent ICP-MS and UV-Vis analyses of the filtrate revealed near-complete Cr removal (>95%) alongside efficient *p*-NPP decomposition through catalysis (Figure 6g).

Finally, we moved to use real environment pollutant for the evaluation of our nanozyme MMM's performance. Paraoxon, one of the most potent acetylcholinesterase-inhibiting insecticides available, ~70% as potent as the nerve agent sarin, is likely an appropriate substrate for the MSN(CeO_2)@PBLG nanozyme (Figure 6h). Given the toxicity of such phosphate nerve agents and the risk in handling them, we used a less toxic analog, methyl paraoxon [56], for a similar evaluation using the nanozyme-integrated MMM. The results were encouraging: as shown in Figure 6i, three consecutive MMM passing-throughs (flow rate ca. 5 mL/min) of a methyl paraoxon solution (10 μM) at 65°C led to ~70% detoxification. Such catalytic decomposition was neither conflicting with adsorption-based pollutant removal, as indicated by the simultaneous Cr removal when $K_2Cr_2O_7$ (0.008 mg/mL) was present in the model solution passing through the MMM. These results clearly highlighted such nanozyme MMM's versatility, and the potential to utilize its functions synergistically for better performance in complex multicomponent systems, such as in a wastewater treatment apparatus.

3 | Conclusion

With the aid of the autocatalyzed NCA-ROP, we were able to prepare the polypeptide-fused NP@PBLG nanocatalyst scaffold with ease. We believe that the introduction of such a platform provides a potential solution to two long-standing challenges in nanocatalyst research: limited catalytic diversity and poor material processability. For the former, we demonstrated four catalytic functions that could be modularly incorporated into the NP@PBLG scaffold, namely NCA-ROP catalysis, Pd-mediated Suzuki coupling, CuAAC, and CeO_2-mediated dephosphorylation. Among them, NCA-ROP catalysis is an unprecedented one, showcasing the first example of nanocatalyst-mediated polypeptide synthesis. For the latter, we showcased the MMM preparation using MSN(CeO_2)@PBLG on Nylon substrate, and the resulting material was successfully utilized as a versatile filtration device to remove aqueous pollutants through both absorptive and catalytic pathways. There is still vast potential for function expansion for this platform, as indicated by our preliminary results (Figures S32–S34) which showed activities similar to Fenton catalyst (with Fe centers), superoxide dismutase (SOD), and peroxidase (POD) (with Au or Pt centers). Crucially, this platform retains the intrinsic advantages of nanozymes and other nanocatalysts: cost-effectiveness, stability, and durability, but has dedicated to address their historical limitations. By bridging inorganic nanocatalysis with nanomaterial engineering and polymer chemistry, we believe that this work has the potential to bring new inspirations for developing versatile nanocatalysts adaptable in different material systems suitable for use in the fields of materials science, biotechnology, environmental science, and beyond, as robust alternatives to natural enzymes and small molecular catalysts.

Acknowledgments

Funding support from the National Natural Science Foundation of China (grant nos. 22361142830, 22374071, 92475101) and the Natural Science Foundation of Hunan Province (grant no. 2024JJ2010) is gratefully acknowledged. The authors thank the Analysis and Testing Center of Hunan University for assistance in characterization. Y.B. thanks his cat Milky for the over 15 years of lovely companionship.

Conflicts of Interest

The authors declare no conflicts of interest.

Data Availability Statement

The data that support the findings of this study are available in the supplementary material of this article.

References

1. L. Gao, J. Zhuang, L. Nie, et al., "Intrinsic Peroxidase-Like Activity of Ferromagnetic Nanoparticles," *Nature Nanotechnology* 2 (2007): 577–583, https://doi.org/10.1038/nnano.2007.260.

2. Y. Zhang, G. Wei, W. Liu, et al., "Nanozymes for Nanohealthcare," *Nature Reviews Methods Primers* 4 (2024): 36, https://doi.org/10.1038/s43586-024-00315-5.

3. Y. Huang, J. Ren, and X. Qu, "Nanozymes: Classification, Catalytic Mechanisms, Activity Regulation, and Applications," *Chemical Reviews* 119 (2019): 4357–4412, https://doi.org/10.1021/acs.chemrev.8b00672.

4. X. Jia, E. Wang, and J. Wang, "Rational Design of Nanozymes for Engineered Cascade Catalytic Cancer Therapy," *Chemical Reviews* 125 (2025): 2908–2952, https://doi.org/10.1021/acs.chemrev.4c00882.

5. M. Liang and X. Yan, "Nanozymes: From New Concepts, Mechanisms, and Standards to Applications," *Accounts of Chemical Research* 52 (2019): 2190–2200, https://doi.org/10.1021/acs.accounts.9b00140.

6. S. Li, Y. Men, Z. Wang, et al., "Amplifying Antigen-Induced Cellular Responses With Proximity Labelling," *Nature* 647 (2025): 506–516, https://doi.org/10.1038/s41586-025-09518-6.

7. V. G. Panferov, X. Zhang, K.-Y. Wong, J. H. Lee, and J. Liu, "Biomedical Applications of Nanozymes: An Enzymology Perspective," *Angewandte Chemie International Edition* 64 (2025): e202512409, https://doi.org/10.1002/anie.202512409.

8. X. Xu, M. Ma, X. Zhou, X. Zhao, D. Feng, and L. Zhang, "Portable Hydrogel Kits Made With Bimetallic Nanozymes for Point-of-Care Testing of Perfluorooctanesulfonate," *ACS Applied Materials & Interfaces* 16 (2024): 15959–15969, https://doi.org/10.1021/acsami.4c00844.

9. X. Liu, X. Mei, J. Yang, and Y. Li, "Hydrogel-Involved Colorimetric Platforms Based on Layered Double Oxide Nanozymes for Point-of-Care Detection of Liver-Related Biomarkers," *ACS Applied Materials & Interfaces* 14 (2022): 6985–6993, https://doi.org/10.1021/acsami.1c21578.

10. J. Yang, B. Pan, F. Zeng, et al., "Magnetic Colloid Antibodies Accelerate Small Extracellular Vesicles Isolation for Point-of-Care Diagnostics," *Nano Letters* 21 (2021): 2001–2009, https://doi.org/10.1021/acs.nanolett.0c04476.

11. F. Cao, L. Jin, Y. Gao, et al., "Artificial-Enzymes-Armed Bifidobacterium Longum Probiotics for Alleviating Intestinal Inflammation and Microbiota Dysbiosis," *Nature Nanotechnology* 18 (2023): 617–627, https://doi.org/10.1038/s41565-023-01346-x.

12. Z. Tu, Y. Zhong, H. Hu, et al., "Design of Therapeutic Biomaterials to Control Inflammation," *Nature Reviews Materials* 7 (2022): 557–574, https://doi.org/10.1038/s41578-022-00426-z.

13. Z. Chen, Y. Yu, Y. Gao, and Z. Zhu, "Rational Design Strategies for Nanozymes," *ACS Nano* 17 (2023): 13062–13080, https://doi.org/10.1021/acsnano.3c04378.

14. C. Wang, M. Zhang, L. Bai, P. Gai, and F. Li, "Light-Driven Self-Cascade Peroxidase-Like Nanozymes Without Exogenous H_2O_2," *Analytical Chemistry* 95 (2023): 7014–7020, https://doi.org/10.1021/acs.analchem.3c00627.

15. Q. Wang, C. Cheng, S. Zhao, et al., "A Valence-Engineered Self-Cascading Antioxidant Nanozyme for the Therapy of Inflammatory Bowel Disease," *Angewandte Chemie International Edition* 61 (2022): e202201101, https://doi.org/10.1002/anie.202201101.

16. K. Kwon, J. Jung, A. Sahu, and G. Tae, "Nanoreactor for Cascade Reaction Between SOD and CAT and its Tissue Regeneration Effect," *Journal of Controlled Release* 344 (2022): 160–172, https://doi.org/10.1016/j.jconrel.2022.02.033.

17. Y. Li, P. Wang, L. Huang, et al., "Schiff-Base Chemistry-Coupled Catechol Oxidase-Like Nanozyme Reaction as a Universal Sensing Mode for Ultrasensitive Biosensing," *Analytical Chemistry* 95 (2023): 3769–3778, https://doi.org/10.1021/acs.analchem.2c04897.

18. J. Chen, Q. Ma, M. Li, et al., "Glucose-Oxidase Like Catalytic Mechanism of Noble Metal Nanozymes," *Nature Communications* 12 (2021): 3375, https://doi.org/10.1038/s41467-021-23737-1.

19. Z.-Y. Liao, W.-W. Gao, N.-N. Shao, et al., "Iron Phosphate Nanozyme–Hydrogel With Multienzyme-Like Activity for Efficient Bacterial Sterilization," *ACS Applied Materials & Interfaces* 14 (2022): 18170–18181, https://doi.org/10.1021/acsami.2c02102.

20. Q. Li, M. Dong, Q. Han, et al., "Enhancing Diabetic Wound Healing With a pH-Responsive Nanozyme Hydrogel Featuring Multi-Enzyme-Like Activities and Oxygen Self-Supply," *Journal of Controlled Release* 365 (2024): 905–918, https://doi.org/10.1016/j.jconrel.2023.12.015.

21. C. Xu, W. Bing, F. Wang, J. Ren, and X. Qu, "Versatile Dual Photoresponsive System for Precise Control of Chemical Reactions," *ACS Nano* 11 (2017): 7770–7780, https://doi.org/10.1021/acsnano.7b01450.

22. C. Hu, R. Man, H. Li, M. Xia, Z. Yu, and B. Tang, "Near-Infrared Triggered Self-Accelerating Nanozyme Camouflaged With a Cancer Cell Membrane for Precise Targeted Imaging and Enhanced Cancer Immunotherapy," *Analytical Chemistry* 95 (2023): 13575–13585, https://doi.org/10.1021/acs.analchem.3c02218.

23. D. W. Bradbury, M. Azimi, A. J. Diaz, et al., "Automation of Biomarker Preconcentration, Capture, and Nanozyme Signal Enhancement on Paper-Based Devices," *Analytical Chemistry* 91 (2019): 12046–12054, https://doi.org/10.1021/acs.analchem.9b03105.

24. L. Feng, Z. Dong, C. Liang, et al., "Iridium Nanocrystals Encapsulated Liposomes as Near-Infrared Light Controllable Nanozymes for Enhanced Cancer Radiotherapy," *Biomaterials* 181 (2018): 81–91, https://doi.org/10.1016/j.biomaterials.2018.07.049.

25. F. Zhang, K. Cheng, Z. Y. Huang, et al., "Tumor Microenvironment-Responsive Nanocarrier Based on VO_x Nanozyme Amplify Oxidative Stress for Tumor Therapy," *Advanced Functional Materials* 33 (2023): 2212740, https://doi.org/10.1002/adfm.202212740.

26. H. Li, T. Wang, Y. Wang, S. Wang, P. Su, and Y. Yang, "Intrinsic Triple-Enzyme Mimetic Activity of V_6O_{13} Nanotextiles: Mechanism Investigation and Colorimetric and Fluorescent Detections," *Industrial & Engineering Chemistry Research* 57 (2018): 2416–2425, https://doi.org/10.1021/acs.iecr.7b04821.

27. I. Safarik, J. Prochazkova, M. A. Schroer, et al., "Cotton Textile/Iron Oxide Nanozyme Composites With Peroxidase-Like Activity: Preparation, Characterization, and Application," *ACS Applied Materials & Interfaces* 13 (2021): 23627–23637, https://doi.org/10.1021/acsami.1c02154.

28. S. Liu, Y. Wang, Y. Zhao, et al., "A Nanozyme-Based Electrode for High-Performance Neural Recording," *Advanced Materials* 36 (2023): 2304297, https://doi.org/10.1002/adma.202304297.

29. D. Zheng, Y. Zheng, J. Tan, Z. Zhang, H. Huang, and Y. Chen, "Co-Immobilization of Whole Cells and Enzymes by Covalent Organic Framework for Biocatalysis Process Intensification," *Nature Communications* 15 (2024): 5510, https://doi.org/10.1038/s41467-024-49831-8.

30. X. Wang, X. Wang, X. Bai, et al., "Nanoparticle Ligand Exchange and Its Effects at the Nanoparticle–Cell Membrane Interface," *Nano Letters* 19 (2018): 8–18, https://doi.org/10.1021/acs.nanolett.8b02638.

31. R. S. Fernandes, I. M. Raimundo, and M. F. Pimentel, "Revising the Synthesis of Stöber Silica Nanoparticles: A Multivariate Assessment Study on the Effects of Reaction Parameters on the Particle Size," *Colloid Surface A* 577 (2019): 1–7, https://doi.org/10.1016/j.colsurfa.2019.05.053.

32. P. Singh, S. Srivastava, and S. K. Singh, "Nanosilica: Recent Progress in Synthesis, Functionalization, Biocompatibility, and Biomedical Applications," *ACS Biomaterials Science and Engineering* 5 (2019): 4882–4898, https://doi.org/10.1021/acsbiomaterials.9b00464.

33. D. R. Radu, C.-Y. Lai, K. Jeftinija, E. W. Rowe, S. Jeftinija, and V. S.-Y. Lin, "A Polyamidoamine Dendrimer-Capped Mesoporous Silica Nanosphere-Based Gene Transfection Reagent," *Journal of the American Chemical Society* 126 (2004): 13216–13217, https://doi.org/10.1021/ja046275m.

34. S. P. Naik, S. P. Elangovan, T. Okubo, and I. Sokolov, "Morphology Control of Mesoporous Silica Particles," *Journal of Physical Chemistry C* 111 (2007): 11168–11173, https://doi.org/10.1021/jp072184a.

35. M. Wu, Y. Chen, L. Zhang, et al., "A Salt-Assisted Acid Etching Strategy for Hollow Mesoporous Silica/Organosilica for pH-Responsive Drug and Gene Co-Delivery," *Journal of Materials Chemistry B* 3 (2015): 766–775, https://doi.org/10.1039/C4TB01581A.

36. H. Kukula, H. Schlaad, M. Antonietti, and S. Förster, "The Formation of Polymer Vesicles or "Peptosomes" by Polybutadiene- block -poly(l -glutamate)s in Dilute Aqueous Solution," *Journal of the American Chemical Society* 124 (2002): 1658–1663, https://doi.org/10.1021/ja012091l.

37. Y. Geng, D. E. Discher, J. Justynska, and H. Schlaad, "Grafting Short Peptides Onto Polybutadiene- block -poly(Ethylene Oxide): A Platform for Self-Assembling Hybrid Amphiphiles," *Angewandte Chemie*

International Edition 45 (2006): 7578–7581, https://doi.org/10.1002/anie.200602739.

38. C. Zhang, W. Wu, R. Q. Li, et al., "Peptide-Based Multifunctional Nanomaterials for Tumor Imaging and Therapy," *Advanced Functional Materials* 28 (2018): 1804492, https://doi.org/10.1002/adfm.201804492.

39. C. Schatz, S. Louguet, J.-F. Le Meins, and S. Lecommandoux, "Polysaccharide- block -polypeptide Copolymer Vesicles: Towards Synthetic Viral Capsids," *Angewandte Chemie International Edition* 48 (2009): 2572–2575, https://doi.org/10.1002/anie.200805895.

40. H. Q. Song, Y. Fan, Y. Hu, G. Cheng, and F. J. Xu, "Polysaccharide–Peptide Conjugates: A Versatile Material Platform for Biomedical Applications," *Advanced Functional Materials* 31 (2020): 2005978, https://doi.org/10.1002/adfm.202005978.

41. W. Ke, J. Li, F. Mohammed, et al., "Erythrocyte Membrane Cloaked Metal–Organic Framework Nanoparticle as Biomimetic Nanoreactor for Starvation-Activated Colon Cancer Therapy," *ACS Nano* 13 (2019): 2357–2369.

42. R. Baumgartner, H. Fu, Z. Song, Y. Lin, and J. Cheng, "Cooperative Polymerization of α-Helices Induced by Macromolecular Architecture," *Nature Chemistry* 9 (2017): 614–622, https://doi.org/10.1038/nchem.2712.

43. C. Chen, H. Fu, R. Baumgartner, Z. Song, Y. Lin, and J. Cheng, "Proximity-Induced Cooperative Polymerization in "Hinged" Helical Polypeptides," *Journal of the American Chemical Society* 141 (2019): 8680–8683, https://doi.org/10.1021/jacs.9b02298.

44. Z. Song, H. Fu, J. Wang, et al., "Synthesis of Polypeptides via Bioinspired Polymerization of in Situ Purified N -carboxyanhydrides," *Pnas* 116 (2019): 10658–10663, https://doi.org/10.1073/pnas.1901442116.

45. S. Lv, H. Kim, Z. Song, et al., "Unimolecular Polypeptide Micelles via Ultrafast Polymerization of N -Carboxyanhydrides," *Journal of the American Chemical Society* 142 (2020): 8570–8574, https://doi.org/10.1021/jacs.0c01173.

46. W. Wang, H. Fu, Y. Lin, J. Cheng, and Z. Song, "Cooperative Covalent Polymerization of N -carboxyanhydrides: From Kinetic Studies to Efficient Synthesis of Polypeptide Materials," *Accounts of Materials Research* 4 (2023): 604–615, https://doi.org/10.1021/accountsmr.3c00046.

47. Q. Wang, X. Cai, Y. Liu, J. Xie, Y. Zhou, and J. Wang, "Pd nanoparticles Encapsulated Into Mesoporous Ionic Copolymer: Efficient and Recyclable Catalyst for the Oxidation of Benzyl Alcohol With O_2 Balloon in Water," *Applied Catalysis B: Environmental* 189 (2016): 242–251, https://doi.org/10.1016/j.apcatb.2016.02.067.

48. M. J. Manto, P. Xie, and C. Wang, "Catalytic Dephosphorylation Using Ceria Nanocrystals," *ACS Catalysis* 7 (2017): 1931–1938, https://doi.org/10.1021/acscatal.6b03472.

49. T. Yao, Z. Tian, Y. Zhang, and Y. Qu, "Phosphatase-Like Activity of Porous Nanorods of CeO_2 for the Highly Stabilized Dephosphorylation Under Interferences," *American Chemical Society Applied Materials & Interfaces* 11 (2019): 195–201, https://doi.org/10.1021/acsami.8b17086.

50. S. Koo, H. S. Sohn, T. H. Kim, et al., "Ceria-Vesicle Nanohybrid Therapeutic for Modulation of Innate and Adaptive Immunity in a Collagen-Induced Arthritis Model," *Nature Nanotechnology* 18 (2023): 1502–1514, https://doi.org/10.1038/s41565-023-01523-y.

51. H. Wu, F. Li, S. Wang, et al., "Ceria Nanocrystals Decorated Mesoporous Silica Nanoparticle Based ROS-Scavenging Tissue Adhesive for Highly Efficient Regenerative Wound Healing," *Biomaterials* 151 (2018): 66–77, https://doi.org/10.1016/j.biomaterials.2017.10.018.

52. M. H. Hassan, D. Andreescu, and S. Andreescu, "Cerium Oxide Nanoparticles Stabilized Within Metal–Organic Frameworks for the Degradation of Nerve Agents," *ACS Applied Nano Materials* 3 (2020): 3288–3294.

53. Z. Zhou, S. Li, G. Wei, et al., "Cerium-Based Metal–Organic Framework With Intrinsic Haloperoxidase-Like Activity for Antibiofilm Formation," *Advanced Functional Materials* 32 (2022): 2206294, https://doi.org/10.1002/adfm.202206294.

54. O. Purikova, I. Tkachenko, B. Šmíd, et al., "Free-Blockage Mesoporous Silica Nanoparticles Loaded With Cerium Oxide as ROS-Responsive and ROS-Scavenging Nanomedicine," *Advanced Functional Materials* 32 (2022): 2208316, https://doi.org/10.1002/adfm.202208316.

55. J. Yang, K. Li, C. Li, and J. Gu, "Intrinsic Apyrase-Like Activity of Cerium-Based Metal–Organic Frameworks (MOFs): Dephosphorylation of Adenosine Tri- and Diphosphate," *Angewandte Chemie International Edition* 59 (2020): 22952–22956, https://doi.org/10.1002/anie.202008259.

56. M. J. Katz, J. E. Mondloch, R. K. Totten, et al., "Simple and Compelling Biomimetic Metal–Organic Framework Catalyst for the Degradation of Nerve Agent Simulants," *Angewandte Chemie International Edition* 53 (2014): 497–501, https://doi.org/10.1002/anie.201307520.

Supporting Information

Additional supporting information can be found online in the Supporting Information section.

Supporting File 1: Supporting Information is available from the Wiley Online Library or from the author.